Nanoscale

High-Performance Field Emission Based on Nanostructured Tin Selenide for Nanoscale Vacuum Transistors

Journal:	*Nanoscale*
Manuscript ID	NR-COM-09-2018-007912.R2
Article Type:	Communication
Date Submitted by the Author:	13-Jan-2019
Complete List of Authors:	Nguyen, Huuduy; University of California, Los Angeles (UCLA), School of Engineering and Applied Science Kang, Joonsang; University of California, Los Angeles (UCLA), School of Engineering and Applied Science Li, Man; University of California, Los Angeles (UCLA), School of Engineering and Applied Science Hu, Yongjie; University of California, Los Angeles (UCLA), School of Engineering and Applied Science

High-Performance Field Emission Based on Nanostructured Tin Selenide for Nanoscale Vacuum Transistors

Huuduy Nguyen, Joon Sang Kang, Man Li, and Yongjie Hu*

School of Engineering and Applied Science,
University of California, Los Angeles, Los Angeles, CA, 90095

*Corresponding author. Email: yhu@seas.ucla.edu

Abstract

Vacuum field effect transistor has been envisioned to hold the promise of replacing solid-state electronics when the ballistic transport of electrons in nanoscale vacuum can enable significantly high switching speed and stability. However, it remains challenging to obtain high-performance and reliable field-emitter materials. In this work, we report a systematic study on field emission of a novel two-dimensional tin selenide (SnSe) with rational design of its structures and surface morphologies. SnSe in the form of atomically-smooth single crystals and nanostructures (nanoflowers) are chemically synthesized and studied as field emitters with varied channel lengths from 6 μm to 100 nm. Our study shows that devices based on the SnSe nanoflowers significantly improve the performance and enables field emission at a reduced voltage due to a surface-enhanced local electrostatic field, and further lead to a nonlinear dependent channel scaling when channel length is smaller than 600 nm. We measured a record-high short-channel field-enhancement factor of 50600 for 100 nm device. Moreover, we investigated the emission stability and measured the fluctuations of the emission current are smaller than 5% for more than 20 hours. Our results demonstrate a high-performance and highly reliable field emitter based on 2D SnSe nanostructures and develop an important building block for nanoscale vacuum field effect transistors.

Solid-state electronics has powered the information technology revolution since the 1960s, however its continuous scaling following the Moore's law is nearing the end due to many intrinsic challenges [1–10]. Beyond the traditional metal-oxide-semiconductor field-effect transistors (MOSFETs), advanced design based on new materials and device operations are needed to further improve the speed and performance. Novel 1D and 2D nanomaterials have been the research focus for last decades and enabled new opportunities. Nanowire [11–15], carbon nanotube [16–19], and graphene transistors [20,21] have been intensively studied. In particular, Ge/Si nanowire heterostructure has been created and enabled high-performance transistors significantly outperforming silicon MOSFETs with a 2-THz intrinsic switching speed with a 40 nm channel length device [11–15]. Other efforts include improving the gate coupling and reducing short-channel effects such as using surrounding gate and FinFETs [22–24] as well as developing new operation paradigms such as tunneling transistors [25], piezoelectronic transistor [26], ferroelectric-gate FET [27], spintronics [13,14,28], and memristors and neuromorphic devices [29,30]. These proposed new devices aimed to circumvent intrinsic limitations of MOSFETs and to lower the transistor's power consumption.

Despite the traditional focus on solid-state electronics, the transport of electrons in vacuum in principle allows for orders of higher velocities than that in the solid state. The high speed operation is also expected at atmospheric pressure under a small anode-cathode gap below the electron mean free paths in air, which leads to a sufficiently low scattering probability between the electrons and gas molecules. For this motivation, more recently, vacuum field effect transistor (VFET) was proposed as an attractive concept beyond solid-state devices. VFET uses vacuum as its channel instead of the traditional doped silicon channel for charge carrier transport; the electrons travel across the vacuum channel via ballistic field emission to enable

high speed. Due to this, VFET is also expected to have high temperature and radiation tolerance; and its operating frequency is expected to be at least ten time higher than traditional MOSFET [31–33]. In addition, by reducing the channel length below the mean free path of electron in air (~ 100 nm), the VFET can be operational in air due to low probability of electrons and air molecules collision [31]; this effectively removes the high vacuum requirement of the VFET. However, experimental efforts on VFET have been scarce. Silicon-based devices are among the first exploration for VFET due to the ease of fabrication [34–38]. These early studies show good promise in building nanoscale vacuum devices but also indicate the needs for materials improvement. In particular, the instability and high turn-on voltage of emitter materials present a major challenge. On the other hand, recent literature efforts in studying new materials for field emission provide useful insight. Diamond is one of the most popular materials for field emission application due to its low work function and negative electron affinity, but diamond suffers from high cost, slow growth rates, low quality, and challenging processing with semiconductors. Carbon nanotube, nanowire, and two dimensional materials such as graphene have been studied because of their high aspect ratio and unique nanoscale geometry for field emission [39–53] . However, for VFET application, a low turn-on voltage and high stability in air need yet to be demonstrated.

Fundamentally, several merits are needed for the ideal VFET emitter material: First, a low work function is desired for low electron tunneling barrier and thereby introduces a small turn-on voltage. Second, materials with high atomic bond energy are desirable to maintain long-term stable field emission and prevent degradation [39]. For these required properties, tin selenide (SnSe) seems to be a good candidate for VFET. SnSe is a 2D material with orthorhombic crystal structure, naturally providing a nanoscale field emission tip down to single atomic layer. The bonding energy of SnSe is ~ 4.16 eV [54], higher than other materials: 3.21 eV for silicon [54], 2.59

eV for ZnO [54], and 2.56 eV for MoS_2 [55]. The work function of SnSe (3.9 eV) [56] is also low considering most studied materials. SnSe has been recently studied for thermoelectric applications due to its record-high figure of merit [57,58]. However, its field emission properties have not been explored so far. Here, we investigated for the first time the field emission performance and stability of SnSe with controlled nanostructure morphologies.

To evaluate the effect of surface morphologies on the field emission performance, we used two different chemical synthesis approaches to control the structures of SnSe in the shape of regular crystals and nanoflowers. First, SnSe single crystals (SCs) with atomically flat crystalline plane surface are prepared via vapor transport method to make a large SnSe crystals (see Supplementary Information). Sn and Se atoms are covalently bond with ~ 3.1 Å bonding length along the in-plane direction and ~2.75 Å along the cross-plane direction [59]; and the layers are weakly bond together by van der Waals force (Figure 1a). The as synthesized SC is large but rough (inset of Figure 1b) which is not suitable for our experiment; therefore, we mechanically exfoliate the crystal to make a flat surface. The SEM image of the exfoliated SC (Figure 1b) reveals the large smooth surface with few broken edges along the in-plane direction of the SnSe crystal. Second, SnSe nanostructure in the structure of flowers, i.e. nanoflowers (NFs) is synthesized using solution reaction method based on ref [60] (see supplementary). In Figure 1c, a single piece of NF has been examined by SEM and clearly shows nanoscale sharp tip that could enhance electric field while the whole sample in cm scale (inset, Figure 1c) reveals a dense flower-like morphology [60] that largely increases surface areas for high power emission with high current density. From the SEM, we estimate the average diameter of a NF particle is around 1.2 μm and the sharp tip is 20~60 nm thick in cross-plane direction and 300~500 nm long in the in-plane direction. Moreover, the SEM images showed the tip of NF is similar to a cylindrical

nanowire that enhances field emission. Such a large aspect ratio between the thickness of the tip and the size of NF indicate that the NF-based emitter would strongly improve emission efficiency. We further use atomic force microscopy (AFM) to characterize the exact surface profile of both SC and NF in order to calculate field enhancement factor. The AFM image of the exfoliated SC revealed a flat surface with roughness below 2 nm (Figure 1d). The AFM data also shows that the surface profile of a NF tip is plane-like structure with forming an emission tip of about 60 nm thick and 300 nm long (Figure 1e). Finally, we use powder X-ray diffraction (XRD) to characterize the crystal lattice structure of our samples. Figure 1f shows sharp peaks we observed are corresponding with orthorhombic SnSe with *Pnma* space group #62 (ICDD #00-014-0159) with lattice constants of 11.5 Å, 4.1 Å, and 4.4 Å in a, b, and c direction respectively. In addition, the sharp peaks in Figure 1f indicate the good crystallinity of our samples.

Next, to investigate the field emission performance of SnSe, we fabricate field emission devices using the two different SnSe samples as the emitter. The field emission measurement of SnSe is configured in diode configurations as shown in Figure 2a. We use oxide insulation layer to control channel length with SnSe as cathode emitter and gold coated glass as anode. To make comparison, we fabricate field emitters based on a single piece of SnSe SC and SnSe NF respectively. SnSe SC cathode was made by exfoliating the crystal to create an atomic smooth surface (top of Figure 2a). SnSe NF cathode was fabricated using ebeam lithography and atomic layer deposition (bottom of Figure 2a). A gold film was used as the anode for both devices, and was deposited by e-beam evaporation. The channel distance was designed using a thin film of aluminum oxide deposited onto the substrate prepared from ebeam evaporation (middle of Figure 2a). This fabrication method effectively creates an 80 μm wide channel with its length controlled by the oxide's thickness. A single field emission device is formed between the gold film and a

SnSe SC/NF tip, and its channel length is verified by SEM. As examples show in Figure 2b and 2c, the channel length between the SnSe and anode is ~100 nm which taken as the distance between two flat surfaces (for SC case) and between the apex of the tip of NF and the flat anode. The SEM images reveal smooth surface of SC while the tip of NF is very sharp parabolic tip with many protrusions.

Next, careful electrical transport measurements were formed on the fabricated devices to evaluate their field emission performance in comparison with other materials and to determine how surface morphology of SC and NF alters the field emission. The samples were measured in air at room temperature and ambient pressure. To initiate field emission we slowly increase the bias DC voltage between the cathode and anode at 0.01 V per increment and record the emission current. The measured field emission J-V curves for SC and NF devices with 100 nm channel are plotted in Figure 3a. The field emission curve is similar to that of a diode device as shown in Figure 3a: the measured current density is small until the bias voltage reaches a turn-on voltage then it begins to exponentially increase. This is originated from vacuum tunneling which requires that the electrons have enough energy at high bias voltage to tunnel across the vacuum barrier via field emission. In general, the field emission was modeled by Fowler-Nordheim (FN) equation given as

$$I = A\frac{aV^2\beta^2}{h^2\varphi}exp\left(-\frac{b\varphi^{1.5}h}{V\beta}\right) \quad (1)$$

where *A* is emitter's effective area, *h* is vacuum channel length between anode and SnSe cathode emitter through which electron tunnel, φ is emitter's work function, β is field enhancement factor which defined as the ratio between local electric field around emitter to the macroscopic applied electric field, and a and b are constant with $a = 1.54 \times 10^{-6}\, A \cdot eV/V^2$ and $b = 6.83 \times 10^9\, eV^{-1.5}Vm^{-1}$. From equation (1), it can be seen that the field emission current is largely

influenced by the work function, field enhancement factor, and channel length. Therefore, small work function and channel length and large field enhancement factor are needed to achieve large emission current with low turn-on voltage. SnSe NF in Figure 3a has higher emission current density in comparison with SC, which is attributed to the parabolic profile of the NF tip where the local electric field is strongly enhanced versus a flat surface. The turn-on voltage is extracted through the linear extrapolation of the J-V curve. From Figure 3a, the turn-on voltage of 100-nm channel NF device is 0.4 V which is significantly lower than literature [34,35]; we attribute this to the small channel length and the low work function of SnSe.

We replot our emission curve in FN plot ($\log(I/V^2)$ vs. $1/V$) in Figure 3b; the prediction lines using FN equation are plotted for comparison, which verifies that field emission is the dominate electron transport mechanism. In Figure 3b, the NF yields two straight lines which indicate two different emission regions; and similarly, the FN plot for SC also yields two straight lines (inset of Figure 3b). To further evaluate performance on field emission, we extract the key performance metrics of field emission devices, more specifically the field enhancement factor. The field enhancement factor from the slopes of linear regions is evaluated by assuming the channel length *h* varies with the emitter's morphology so the FN equation is rewritten as

$$I = \int\int \frac{aV^2\beta^2}{h(x,y)^2\varphi} exp\left(-\frac{b\varphi^{1.5}h(x,y)}{V\beta}\right) dxdy \qquad (2)$$

and the slope of straight line in FN plot is then calculate as

$$\frac{d\left(\ln\left(\frac{I}{V^2}\right)\right)}{d\frac{1}{V}} = \frac{\mathrm{d}\, ln\left(\int\int \frac{\beta^2}{h(x,y)^2} exp\left(-\frac{b\varphi^{1.5}h(x,y)}{V\beta}\right) dxdy\right)}{\mathrm{d}\frac{1}{V}} \quad (3)$$

Assuming only single petal tip emit electron (with area of ~60 nm x 300 nm from Figure 1e) for NF and an arbitrary area for flat surface, by matching experiment data in Figure 3b and morphology of NF tip and SC flat surface, the field enhancement factors of SC are 320 and 76

for first and second regions respectively; and the field enhancement factors of NF are 50600 and 7930 for first and second regions (See supplementary). Interestingly, the field enhancement factor of 50600 measured in NF emitter is record high comparing to the reported literatures with similar channel length [61]. The field enhancement factor of SnSe NF is much larger than SC as expected due to its morphology. However, the first region of SC has an unusual large field enhancement factor considering the emitter is a flat surface; the second region has lower field enhancement factor and is more realistic. This phenomenon has been observed for past decades for other emitters [33,34,62]; the first emission region is most likely originate from the surface roughness we observed in our AFM and SEM measurements (Figure 1b and 1d) and the second region is originate from the combination of the whole flat surface of SC and the roughness. Likewise, the first emission region of NF with record high field enhancement factor of 50600 is due to protrusions we observed in Figure 2c while the second emission region is originate from both protrusions and the NF tip. For 100 nm devices, the ratio of field enhancement factors between the NF and SC is about 158 and 104 respectively for the two emission regions, indicating that the field enhancement contribution from the surface morphology of NF is about 100 times dominant over that from the channel distances.

The extracted high field enhancement factor is attributed to the unique nanostructures and field emission geometry of the SnSe devices. On the other hand, we note that there are physical and mathematical assumptions for typical FN-type equations, i.e. orthodox emission hypothesis [63]. In particular, (i) The emitting surface is treated as uniform voltage; (ii) The measured emission current is equal to the device current; (iii) Emission is treated as deep tunneling through a Schottky-Nordheim barrier with quantities independent on the voltage; (iv)The local work function of the emitter is constant. Additional factors may break these hypotheses and introduce

non-orthodox. For example: The voltage non-uniformity in the emitting regions and surrounding counter-electrodes for non-metal emitters can likely break the condition (i); Possible scattering or leakage that introduce inequality between emission current and measured device current may break the condition (ii); Dependent variables and barrier-form correction factors in the FN-type equation can break the condition (iii); Local surface trapped charge or defects can result in non-uniform work function of the emitter surface and break the condition (iv). Scaling down the tunneling channel or emitter size may make it even hard to satisfy such orthodox due to more stringent geometric requirements at the nanoscale. Therefore, a more sophisticated data-analysis theory can help better understand the field emission mechanisms for novel materials and nanoscale field emission geometries.

To further study the origin of field emission, we use Finite-Element methods to simulate electric field in SC and NF devices (Figure 3c). We model SC as 1 mm thick substrate with a flat surface expose to the anode (top of Figure 3c); and for simplicity, NF tip is modeled as 1.2 μm rod with round tip of 60 nm diameter (bottom of Figure 4c). We set the gap between SnSe and anode to be 100 nm and 0.5 V bias voltages. The simulation shows that electric field concentrates around the apex of NF tip and gradually decreases along the tip's radial direction; on other hand the electric field of SC is uniform for entire surface. The simulation suggests the NF emits electrons first from the tip's apex due to the concentrated field; and as voltage increases the electric field along the radial direction gradually reaches turn-on field thus begin to emit electron. This reflects in our data in Figure 3a in which the emission current is gradually increases with voltage (NF data in Figure 3a). For the SC, the simulation suggests that once the turn-on voltage is reached for the flat surface, the entire surface would emit at once. From the simulation, we can clearly see that NF is better emitter than SC purely due to the morphology of

the NF that concentrates electrostatic field; however, the NF only emits electron from its tip while SC emits electron from its whole flat surface. Thus, NF has higher field enhancement factor than SC.

We further study the channel length dependence of SnSe NF field emission and determine the distance dependence of turn-on voltage and field enhancement factor. Figure 4a shows distance dependence of field emission and Figure 4b shows the FN plot of SnSe NF. The extracted field enhancement factor at the second emission region of NF tip for 100 nm, 250 nm, 600 nm, 3 μm, and 6 μm channel are 7930, 5730, 3010, 6190 and 13800 respectively; and the extracted turn-on voltages are 0.40 V, 1.15 V, 2.32 V, 4.44 V, and 9.87 V respectively. Figure 4a and 4b show that as channel length increases the turn-on voltage is increases due to more voltage required to maintain same electric field.

We also noticed that the non-monochronic channel length dependence of field enhancement factor is observed in our measurement (Figure 4c). The decreases and then increases of field enhancement factor with channel length cannot be simply described using the increasing field enhancement factor at large channel length [64–69]; however, such behavior has been observed in literature for field emission devices with extremely small channels [70–74]. The increases of field enhancement factor at small channel length is due to the local electric field at the tip's apex reaches infinity as the channel length approach zero while the macroscopic electric field far away from the tip reaches a finite value. To qualitatively understand this trend, we consider the empirical field enhancement factor for large channel length greater than few micrometers as [65,68]

$$\beta = Ch + C_0 \quad (4)$$

where h is channel length and C and C_0 are fitting constants. With small channel length less than one micrometer, Edgcombe and Valdre modelled the field enhancement factor as [73,75]

$$\beta = \beta_0 \left\{1 + A\left(\frac{h+l}{h}\right) - B\left(\frac{h}{h+l}\right)\right\} \quad (5)$$

where β_0 is geometry dependence field enhancement factor, l is height of the emitter, and A and B are fitting constants. As mentioned, the equation (4) and (5) are inconsistent with one another; to make the equations consistent, we combine the two equations as

$$\beta = \left\{C_1 + C_2\left(\frac{h+l}{h}\right) - C_3\left(\frac{h}{h+l}\right)\right\} + C_4 h \quad (6)$$

In equation (6), we use fitting constant C_1 instead of β_0 because there is not any theoretical work we aware of to predict the field enhancement factor of NF. We use 1.2 μm as our l; and 4894, 291, 12383, and 3164 as our C_1, C_2, C_3, and C_4 respectively to fit equation (6) fairly well with our data (Figure 4c). As shown in Figure 4c, at large channel length, the linear term dominates and field enhancement factor varies linearly with channel length (black line in Figure 4c); and at small channel length, the non-linear term dominates (blue curve in Figure 4c). The transition point appears when channel length is comparable with emitter's length. Physically, as channel length decreases from large channel length, the enhancement factor linearly decreases because the emission geometry approaches plane to plane geometry. However, at the transition point, the local electric field around the tip increases faster than the macroscopic electric field far away from the tip; thus the field enhancement factor increases. Therefore, in this region, the field enhancement factor is the combination of the deceases of field enhancement factor due to plane to plane transition and the increase of field enhancement factor due to rapid increase of local electric field.

Interestingly, field emission still happen in air with 6 μm channel; we try to measure field emission stability with large channel length but the current quickly decays. This result is well

expected since the channel length is above mean free path of electron in air (~200 nm) [31]. We do not think the reason for current decay is from air ionization since our operate voltage is much smaller than the required breakdown voltages [76–78]. Thus, the current decay is most likely from electrons scatter with air molecule. We also measure emission stability using the 100 nm channel length and observe more stable emission current (Figure 4d). The emission is stable at 3 A/cm^2 for 20 hours with less than ± 5% fluctuations; in comparison, carbon nanotube, MoS_2, and graphene emitters usually have fluctuation on order of ± 10 % for three hours under high vacuum [49,79,80]. We attribute the higher stability of SnSe to small channel length and high bond energy of SnSe. Finally, we compare the performance of SnSe NF with other materials and notice that the SnSe NF devices require lower turn-on voltage (Figure 5a). The reduced turn-on voltage for field emission is due to its intrinsic low work function and high surface-enhanced electrostatic field (Figure 5b), thus provide advantage for small power operations.

In Summary, we demonstrate high-performance and stable field emission of single SnSe nanostructures in air. With the device channel down to 100 nm, we studied field emission from different surface morphology and observed a significant performance improvement of nanoflower surfaces due to the high aspect ratio. Moreover, the SnSe NF requires only 0.5 V bias voltages to facilitate field emission which is lower than most reported works; and such low turn-on voltage is desirable for low power applications. We further investigate the emission of SnSe NF with different channel lengths and conclude the non-monochronic channel length dependence of the field enhancement factor is due to the rapid increase of local electric field at the tip of SnSe NF as the channel length decreases. Our results show that SnSe nanostructured is a promising material for vacuum field emission and underscores the promise of rational materials

design at the nanoscale to develop new building blocks beyond conventional electronics in the post Moorse's law era.

Figure Captions

Figure 1: Structural design and characterization of Tin Selenide (SnSe). (a) Schematic illustration of the 2D crystal structure of SnSe. (b) Scanning electron microscopy image (SEM) of an exfoliated SnSe single-crystal (SC) sample, the scale bar is 50 μm. Inset is an optical image of an as-synthesized crystal; the scale bar is 3 mm. (c) SEM image of a single tip of the SnSe nanoflower (NF); the scale bar is 10 μm. Inset is the NF arrays; the scale bar is 500 nm. (d) Atomic force microscopy (AFM) image of SnSe SC sample. The inset is a one-dimensional surface scan extracted from the AFM image. (e) AFM image along a tip of SnSe NF. On the right is one-dimensional surface profile of the tip, with the red and blue profiles corresponding to dashed red and blue line in the AFM image. (f) Powder X-ray diffraction of SnSe.

Figure 2: Fabrication of the SnSe field emission devices. (a) Schematic of the fabrication process. The SnSe emitter, metal collector, and oxide insulation layer are illustrated respectively in black, blue, and light pink color. Illustrated are fabrication steps using SnSe single crystal (SC) as the emitter (top), gold as the collector (middle), and SnSe nanoflower (NF) as the emitter (bottom). (b) SEM image of a SnSe SC device with a 100 nm channel. The false color is used to highlight SnSe SC (white) and the anode (blue). Scale bar, 250 nm. (c) SEM image of a SnSe NF device with a 100 nm channel. Dash curve illustrates the parabolic profile of a single NF tip. Scale bar, 500 nm.

Figure 3: Field emission measurement of 100 nm channel SnSe devices. (a) J-V curves of 100 nm channel devices using SnSe SC (blue) and NF (red) as the emitter. (b) The Fowler-Nordheim (FN) plot of SC showed two emission regions. Inset is FN plot of NF. The dash line represents linear fit of the emission regions. (c) The electrostatic field simulated with COMSOL for SC (top) and a tip of NF (bottom).

Figure 4: Field emission measurement of SnSe nanoflower (NF) devices with channel length scaling. (a) Field emission J-V data of SnSe NF devices with channel from 6 μm to 100 nm. (b) The Fowler Nordheim plot of the measured field emission of SnSe NF devices with different channel lengths. (c) Field enhancement factor (β) from measurement (red dot) and empirical fitting (red line) as a function of channel lengths. The contribution of linear and non-linear terms in equation (6) are plotted in black and blue line respectively. (d) Emission stability over 20 hour at 3 A/cm^2 for the 100-nm channel SnSe NF device.

Figure 5: Performance comparison between this work and reported literatures. (a) The turn-on fields and (b) the field enhancement factors of SnSe devices are plotted with channel length dependence, in comparison with data from literatures.

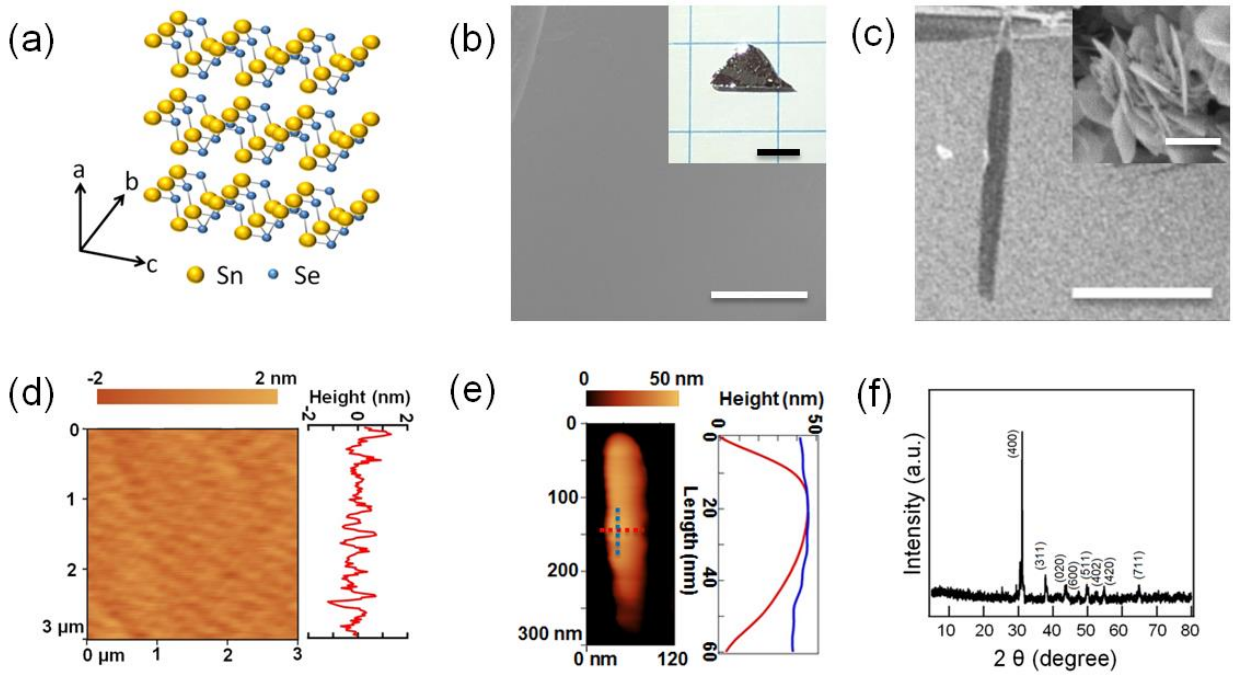
(a)
a
b
c
Sn
Se
(b)
(c)
(d)
-2
2 nm
Height (nm)
0
1
2
3 μm
0 μm
1
2
3
(e)
0
50 nm
Height (nm)
100
200
300 nm
0 nm
120
Length (nm)
20
40
60
(f)
Intensity (a.u.)
(400)
(311)
(020)
(600)
(511)
(402)
(420)
(711)
10
20
30
40
50
60
70
80
2 θ (degree)

Figure 1

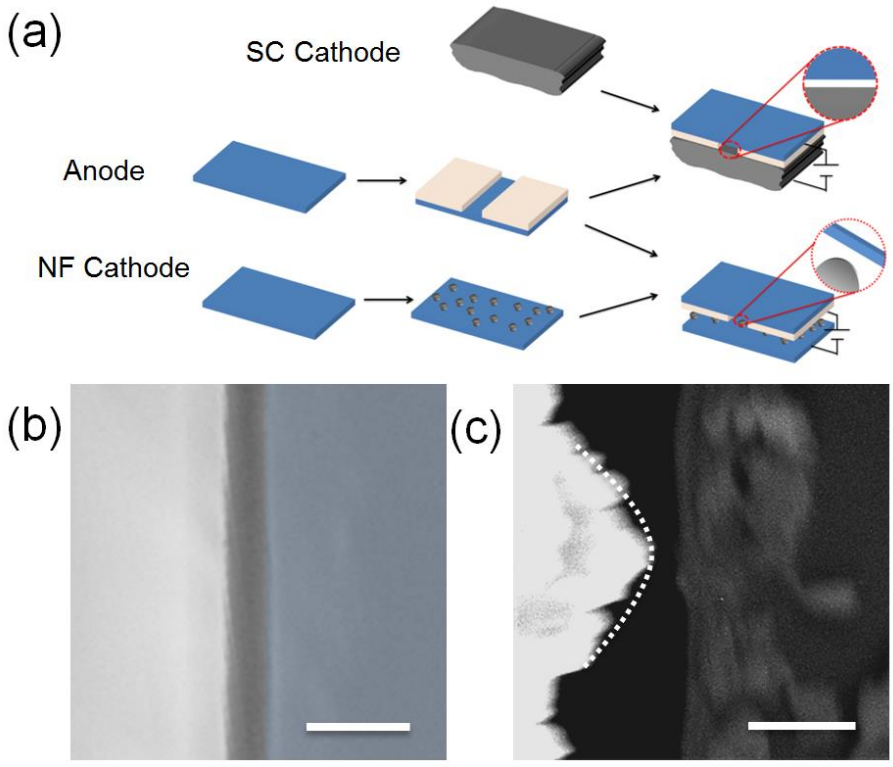

Figure 2

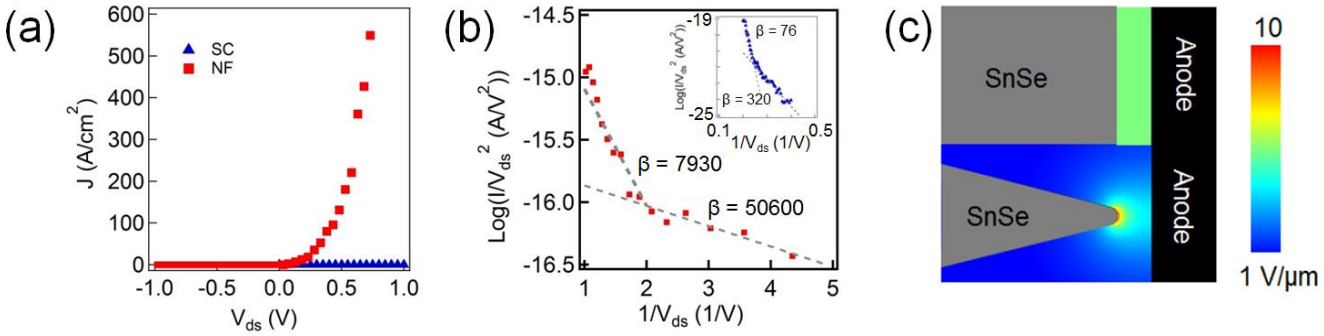
(a)
SC
NF
J (A/cm^2)
V_{ds} (V)
(b)
Log(I/V_{ds}^2 (A/V^2))
1/V_{ds} (1/V)
β = 7930
β = 50600
β = 76
β = 320
(c)
SnSe
Anode
SnSe
Anode
10
1 V/μm

Figure 3

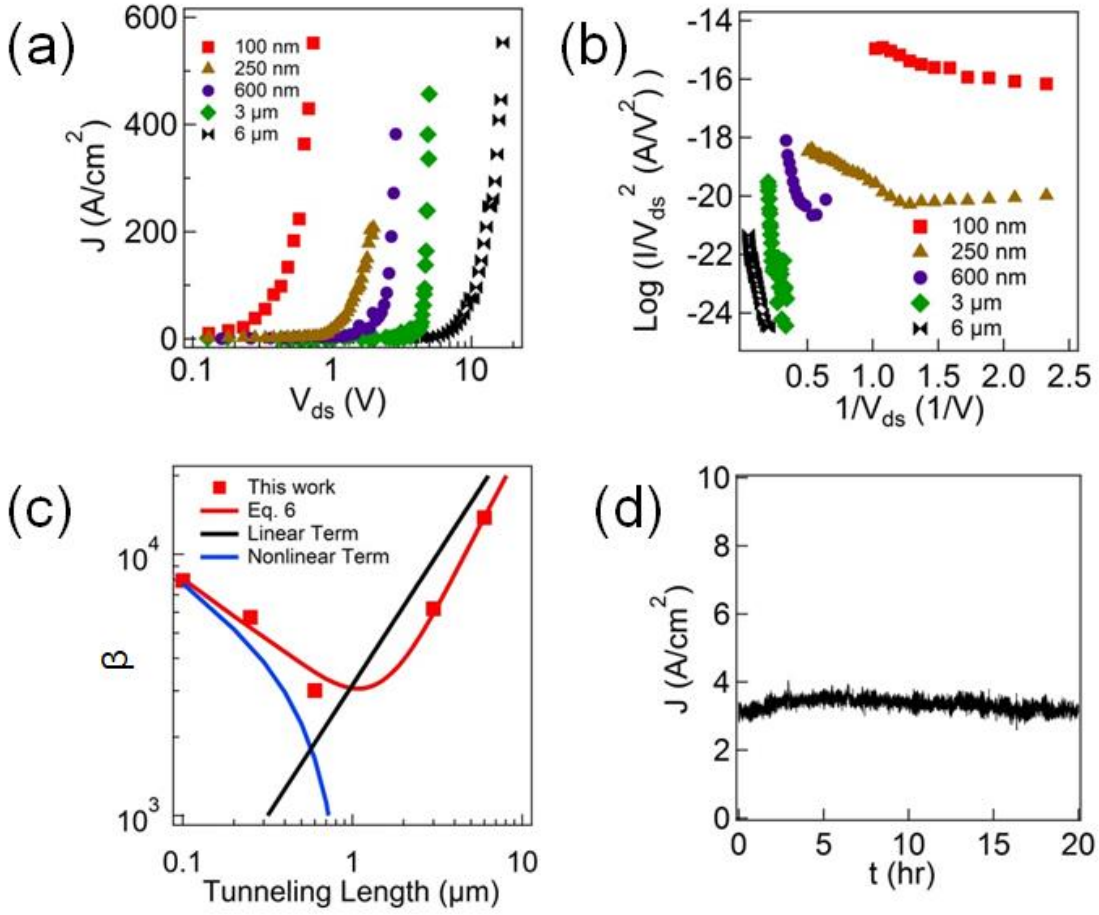
(a)
J (A/cm^2)
V_{ds} (V)
100 nm
250 nm
600 nm
3 μm
6 μm
(b)
Log (I/V_{ds}^2 (A/V^2))
1/V_{ds} (1/V)
100 nm
250 nm
600 nm
3 μm
6 μm
(c)
This work
Eq. 6
Linear Term
Nonlinear Term
β
Tunneling Length (μm)
(d)
J (A/cm^2)
t (hr)

Figure 4

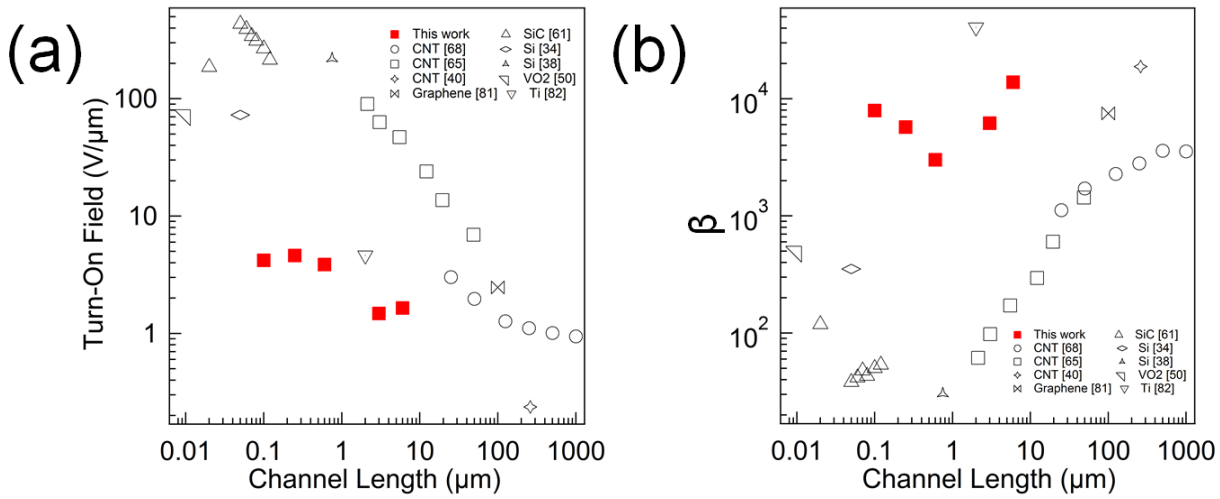
(a)
Turn-On Field (V/μm)
100
10
1
0.01
0.1
1
10
100
1000
Channel Length (μm)
This work
CNT [68]
CNT [65]
CNT [40]
Graphene [81]
SiC [61]
Si [34]
Si [38]
VO2 [50]
Ti [82]
(b)
β
10^4
10^3
10^2
0.01
0.1
1
10
100
1000
Channel Length (μm)
This work
CNT [68]
CNT [65]
CNT [40]
Graphene [81]
SiC [61]
Si [34]
Si [38]
VO2 [50]
Ti [82]

Figure 5

Reference

1. M. Waldrop, *Nature*, 2016, **530**, 144–147.
2. International Technology Roadmap for Semiconductors, *ITRS 2.0 2015 Ed.*, www.itrs2.net/.
3. J. S. Kang, M. Li, H. Wu, H. Nguyen and Y. Hu, *Science*, 2018, **361**, 575–578.
4. T. N. Theis and P. M. Solomon, *Science*, 2010, **327**, 1600–1601.
5. A. D. Franklin, *Science*, 2015, **349**, aab2750.
6. W. Lu and C. M. Lieber, *Nat. Mater.*, 2007, **6**, 841–850.
7. R. Chau, B. Doyle, S. Datta, J. Kavalieros and K. Zhang, *Nat. Mater.*, 2007, **6**, 810–812.
8. M. Lundstrom, *Science*, 2003, **299**, 210–211.
9. M. Luisier, M. Lundstrom, D. A. Antoniadis and J. Bokor, *Int. Electron Devices Meet. (EDM), 2011 IEEE Int.*, 11.2. 1-11.2.4.
10. J. S. Kang, H. Wu and Y. Hu, *Nano Lett.*, 2017, **17**, 7507–7514.
11. Y. Hu, J. Xiang, G. Liang, H. Yan and C. M. Lieber, *Nano Lett.*, 2008, **8**, 925–930.
12. J. Xiang, W. Lu, Y. Hu, Y. Wu, H. Yan and C. M. Lieber, *Nature*, 2006, **441**, 489–493.
13. Y. Hu, H. O. H. Churchill, D. J. Reilly, J. Xiang, C. M. Lieber and C. M. Marcus, *Nat. Nanotechnol.*, 2007, **2**, 622–625.
14. Y. Hu, F. Kuemmeth, C. M. Lieber and C. M. Marcus, *Nat. Nanotechnol.*, 2012, **7**, 47–50.
15. H. Yan, H. S. Choe, S. Nam, Y. Hu, S. Das, J. F. Klemic and J. C. Ellenbogen, *Nature*, 2011, **470**, 240–244.
16. Q. Cao, J. Tersoff, D. B. Farmer, Y. Zhu and S. Han, *Science*, 2017, **356**, 1369–1372.
17. C. Qiu, Z. Zhang, M. Xiao, Y. Yang, D. Zhong and L. Peng, *Science*, 2017, **355**, 271–276.
18. Z. Zhong, N. M. Gabor, J. E. Sharping, A. L. Gaeta and P. L. Mceuen, *Nat. Nanotechnol.*, 2008, **3**, 201–205.
19. A. Javey, J. Guo, Q. Wang, M. Lundstrom and H. Dai, *Nature*, 2003, **424**, 654–657.
20. L. Liao, Y. Lin, M. Bao, R. Cheng, J. Bai, Y. Liu, Y. Qu, K. L. Wang, Y. Huan and X. Duan, *Nature*, 2010, **467**, 305–308.
21. K. S. Novoselov, A. K. Geim, S. V. Morozov, D. Jiang, Y. Zhang, S. V. Dubonos, I. V. Grigorieva and A. A. Firsov, *Science*, 2004, **306**, 666–669.
22. D. Hisamoto, W. Lee, J. Kedzierski, H. Takeuchi, K. Asano, C. Kuo, E. Anderson, T.

King, J. Bokor and C. Hu, *IEEE Trans. Electron Devices*, 2000, **47**, 2320–2325.

23. H. S. P. Wong, *IBM J. RES. DEV.*, 2002, **46**, 133-168.

24. H. Tsai, J. W. Pitera, H. Miyazoe, S. Bangsaruntip, S. U. Engelmann, C. Liu, J. Y. Cheng, J. J. Bucchignano, D. P. Klaus, E. A. Joseph, D. P. Sanders, M. E. Colburn and M. A. Guillorn, *ACS Nano*, 2014, **8**, 5227–5232.

25. D. Sarkar, X. Xie, W. Liu, W. Cao, J. Kang, Y. Gong, S. Kraemer, P. M. Ajayan and K. Banerjee, *Nature*, 2015, **526**, 91–95.

26. D. M. Newns, B. G. Elmegreen, X. Liu and G. J. Martyna, *Adv. Mater.*, 2012, **24**, 3672–3677.

27. S. Salahuddin and S. Datta, *Nano Lett.*, 2008, **8**, 405–410.

28. D. A. Allwood, G. Xiong, C. C. Faulkner, D. Atkinson, D. Petit and R. P. Cowburn, *Science*, 2005, **309**, 1688–1693.

29. J. J. Yang, D. B. Strukov and D. R. Stewart, *Nat. Nanotechnol.*, 2013, **8**, 13–24.

30. S. H. Jo, T. Chang, I. Ebong, B. B. Bhadviya, P. Mazumder and W. Lu, *Nano Lett.*, 2010, **10**, 1297–1301.

31. J. Han and M. Meyyappan, *IEEE Spectr.*, 2014, **51**, 31–35.

32. B. R. Stoner and J. T. Glass, *Nat. Nanotechnol.*, 2012, **7**, 485–487.

33. T. Utsumi, *IEEE Trans. Electron Devices*, 1991, **38**, 2276–2283.

34. J. Han, D. Moon and M. Meyyappan, *Nano Lett.*, 2017, **17**, 2146–2151.

35. J. Han, J. S. Oh and M. Meyyappan, *IEEE Trans. Nanotechnol.*, 2014, **13**, 464–468.

36. S. Srisonphan, Y. S. Jung and H. K. Kim, *Nat. Nanotechnol.*, 2012, **7**, 504–508.

37. B. L. Pescini, A. Tilke, R. H. Blick, H. Lorenz, J. P. Kotthaus, W. Eberhardt and D. Kem, *Adv. Mater.*, 2001, **13**, 1780–1783.

38. C. A. Spindt, C. E. Holland, A. Rosengreen and I. Brodie, *IEEE Trans. Electron Devices*, 1991, **38**, 2355–2363.

39. P. Hou, C. Liu and H. Cheng, in *Nanomaterials Handbook, Second Edition*, 2017, pp. 255–272.

40. S. H. Jo, D. Z. Wang, J. Y. Huang, W. Z. Li, K. Kempa and Z. F. Ren, *Appl. Phys. Lett.*, 2004, **85**, 4.

41. S. Kumar, G. S. Duesberg, R. Pratap and S. Raghavan, *Appl. Phys. Lett.*, 2014, **105**, 5.

42. D. Ye, S. Moussa, J. D. Ferguson, A. A. Baski and M. S. El-shall, *Nano Lett.*, 2012, **12**, 1265–1268.

43. Z. Wu, S. Pei, W. Ren, D. Tang, L. Gao, B. Liu, F. Li, C. Liu and H. Cheng, *Adv. Mater.*, 2009, **21**, 1756–1760.

44. D. J. Late, P. A. Shaikh, R. Khare, R. V Kashid, M. Chaudhary, M. A. More and S. B. Ogale, *ACS Appl. Mater. Interfaces*, 2014, **6**, 15881–15888.

45. M. B. Erande, S. R. Suryawanshi, M. A. More and D. J. Late, *Eur. J. Inorg. Chem.*, 2015, **19**, 3102–3107.

46. A. L. Koh, E. Gidcumb, O. Zhou and R. Sinclair, *Nanoscale*, 2016, **8**, 16405–16415.

47. W. B. Choi, D. S. Chung, J. H. Kang, H. Y. Kim, Y. W. Jin, I. T. Han, Y. H. Lee, J. E. Jung, N. S. Lee, G. S. Park and J. M. Kim, *Appl. Phys. Lett.*, 1999, **75**, 3129–3131.

48. B. D. Banerjee, S. H. Jo and Z. F. Ren, *Adv. Mater.*, 2004, **16**, 2028–2032.

49. B. Z. Pan, H. Lai, F. C. K. Au, X. Duan, W. Zhou, W. Shi, N. Wang, C. Lee, N. Wong, S. Lee and S. Xie, *Adv. Mater.*, 2000, **12**, 1186–1190.

50. M. Liu, W. Fu, Y. Yang, T. Li and Y. Wang, *Appl. Phys. Lett.*, 2018, **112**, 5.

51. C. Li, M. T. Cole, W. Lei, K. Qu, K. Ying, Y. Zhang, A. R. Robertson, J. H. Warner, S. Ding, X. Zhang, B. Wang and W. I. Milne, *Adv. Funct. Mater.*, 2014, **24**, 1218–1227.

52. C. S. Rout, P. D. Joshi, R. V Kashid, D. S. Joag, M. A. More, A. J. Simbeck, M. Washington, S. K. Nayak and D. J. Late, *Sci. Rep.*, 2013, **3**, 8.

53. Y. B. Li, Y. Bando and D. Golberg, *Appl. Phys. Lett.*, 2003, **82**, 1962–1964.

54. D. R. Lide, Ed., *Handbook of Chemistry and Physics*, CRC Press, 87th edn., 2006.

55. X. Fan, W. T. Zheng, J. Kuo and D. J. Singh, *J. Phys. Condens. Matter*, 2015, **27**, 5.

56. Z. Cui, X. Wang, Y. Ding and M. Li, *Superlattices Microstruct.*, 2018, **114**, 251–258.

57. H. Ju and J. Kim, *ACS Nano*, 2016, **10**, 5730–5739.

58. L.-D. Zhao, S.-H. Lo, Y. Zhang, H. Sun, G. Tan, C. Uher, C. Wolverton, V. P. Dravid and M. G. Kanatzidis, *Nature*, 2014, **508**, 373–377.

59. I. Loa, R. J. Husband, R. A. Downie, S. R. Popuri and J. G. Bos, *J. Phys. Condens. Matter*, 2015, **27**, 7.

60. L. Li, Z. Chen, Y. Hu, X. Wang, T. Zhang, W. Chen and Q. Wang, *J. Am. Chem. Soc.*, 2013, **135**, 1213–1216.

61. M. Liu, T. Li and Y. Wang, *J. Vac. Sci. Technol. B, Nanotechnol. Microelectron. Mater. Process. Meas. Phenom.*, 2017, **35**, 5.

62. I. Brodie, *J. Appl. Phys.*, 1964, **35**, 2324–2332.

63. R. G. Forbes, *Proceeding R. Soc. A.*, 2013, **469**, 16.

64. T. Cheng, P. Chen and S. Wu, *Nanoscale Res. Lett.*, 2012, **7**, 6.

65. Z. Xu, X. D. Bai and E. G. Wang, *Appl. Phys. Lett.*, 2006, **23**, 3.

66. R. C. Smith, J. D. Carey, R. D. Forrest and S. R. P. Silva, *J. Vac. Sci. Technol. B Microelectron. Nanom. Struct. Process. Meas. Phenom.*, 2005, **23**, 632–635.

67. R. C. Smith, D. C. Cox and S. R. P. Silva, *Appl. Phys. Lett.*, 2005, **87**, 3.

68. J. Bonard, M. Croci, I. Arfaoui, O. Noury, D. Sarangi and A. Chatelain, *Diam. Relat. Mater.*, 2002, **11**, 763–768.

69. L. Nilsson, O. Groening, C. Emmenegger, O. Kuettel, E. Schaller, L. Schlapbach, H. Kind, J. Bonard and K. Kern, *Appl. Phys. Lett.*, 2000, **76**, 2071–2073.

70. P. Zhang, S. B. Fairchild, T. C. Back and Y. Luo, *AIP Adv.*, 2017, **7**, 6.

71. J. Lin, P. Y. Wong, P. Yang, Y. Y. Lau, W. Tang and P. Zhang, *J. Appl. Phys.*, 2017, **121**, 6.

72. J. Bonard, K. A. Dean, B. F. Coll and C. Klinke, *Phys. Rev. Lett.*, 2002, **19**, 4.

73. C. J. Edgcombe and U. Valdre, *J. Microsc.*, 2001, **203**, 188–194.

74. F. M. Charbonnier, W. A. Mackie, R. L. Hartman and T. Xie, *J. Vac. Sci. Technol. B Microelectron. Nanom. Struct. Process. Meas. Phenom.*, 2001, **19**, 1064–1072.

75. C. J. Edgcombe and U. Valdre, *Philos. Mag.*, 2002, **82**, 987–1007.

76. A. Peschot, N. Bonifaci, O. Lesaint, C. Valadares and C. Poulain, *Appl. Phys. Lett.*, 2014, **105**, 4.

77. Y. Hirata, K. Ozaki, U. Ikeda and M. Mizoshiri, *Thin Solid Films*, 2007, **515**, 4247–4250.

78. E. Hourdakis, G. W. Bryant and N. M. Zimmerman, *J. Appl. Phys.*, 2006, **100**, 6.

79. R. V Kashid, D. J. Late, S. S. Chou, Y. Huang, M. De, D. S. Joag, M. A. More and V. P. Dravid, *small*, 2013, **9**, 2730–2734.

80. W. Heer, A. Chatelain and U. Ugarte, *Science*, 1995, **270**, 1179–1180.

81. A. Malesevic, R. Kemps, A. Vanhulsel, M. P. Chowdhury, A. Volodin and C. Van Haesendonck, *J. Appl. Phys.*, 2008, **104**, 6.

82. S. Pennisi, G. Castorina and D. Patti, *IEEE Trans. Electron Devices*, 2015, **62**, 4293–4300.

Table of Contents Entry

Rational design of two-dimensional tin selenide (SnSe) nanostructures enables high-performance field emission for developing nanoscale vacuum transistors.